Diagnosis of Airspeed Measurement Faults for Unmanned Aerial Vehicles

Søren Hansen and Mogens Blanke *SM IEEE*

Abstract—Airspeed sensor faults are common causes for incidents with unmanned aerial vehicles with pitot tube clogging or icing being the most common causes. Timely diagnosis of such faults or other artifacts in signals from airspeed sensing systems could potentially prevent crashes. This paper employs parameter adaptive estimators to provide analytical redundancies and a dedicated diagnosis scheme is designed. Robustness is investigated on sets of flight data to estimate distributions of test statistics. The result is robust diagnosis with adequate balance between false alarm rate and fault detectability.

Index Terms—Aircraft fault detection, Airspeed sensor fault, Fault diagnosis, UAV, Pitot tube defect, Adaptive observer, Change detection

I. INTRODUCTION

A reliable measurement of airspeed is vital to many simple Unmanned Aerial Vehicles (UAV), since the envelope of stable operation becomes narrow for simple autopilots if speed information is in error. Simple UAV autopilots rarely make use of redundant speed measurements both to avoid the added complexity and due to limitations on weight. Ability to diagnose speed sensor faults without adding additional sensors or actuators to the aircraft would hence be very attractive.

Estimating speed by exploiting other sensors onboard could be possible through state estimation techniques. An aircraft can be described by a set of nonlinear equations with a rich set of parameters, but as it is not feasible, to obtain complete parameter sets for small UAVs, for reasons of cost, estimation of states could be based on models where some parameters are roughly known while others require identification. Several parameters depended on states of the aircraft and vary as the operational conditions change, so combined parameter and state estimation would appear useful. When the structure of nonlinearity is known in a nonlinear dynamical system, and stochastic disturbances are not significant, adaptive observers for nonlinear systems may serve the dual purpose of parameter and state estimation. When stochastic issues become significant and local linearization around a state vector is feasible, Extended Kalman filtering (EKF) techniques are preferred. The literature on both approaches is significant. Such estimation requires certain properties of the nonlinear

S. Hansen is with DTU Electrical Engineering, Technical University of Denmark, Elektrovej B. 326, DK-2800 Lyngby, Denmark and Danish Forces Joint UAV Team, Naval Weapons School, Gnibenvej 55, DK-4583 Sjællands Odde. Denmark. (sh@elektro.dtu.dk)

M. Blanke is with DTU Electrical Engineering, Technical University of Denmark, Elektrovej B. 326, DK-2800 Lyngby, Denmark and with the AMOS Centre of Excellence, Institute of Technical Cybernetics, Norwegian University of Science and Technology, NTNU, NO-7491 Trondheim, Norway. (mb@elektro.dtu.dk)

system. Observability is essential, and this is treated for nonlinear observers in [1]. When the system equations are not simple and calculation of Lie derivatives of the system equations are required, this can be cumbersome. A relaxed approach is to ensure asymptotic convergence to zero of the estimation error. For an adaptive observer, global asymptotic stability can be analyzed employing Lyapunov stability results, as done in [2]. Properties of the extended Kalman filter as a combined state and parameter estimator was treated in other classical results, [3] for linear systems and [4] for a class of nonlinear systems. Once alternative estimates of aircraft speed have been obtained, fault diagnosis could be achieved through residual generation and change detection methods could be adopted to obtain robust diagnosis.

Fault detection and isolation (FDI) has been demonstrated for nonlinear systems with a structure similar to that of aircraft propulsion in for instance [5], who used a sliding mode observer, and in [6], where an adaptive observer was employed. Fault detection, isolation and recovery (FDIR) for aircraft and aerospace systems was studied in [7], that included nonlinear control for recovery, in [8] where partial loss of control surfaces was treated and overviews of theoretical diagnostic techniques for general aircraft faults were treated in [9], [10] and [11]. Goupil [12] showed how FDIR techniques are in use in the Airbus 380.

Approaches to FDI for unmanned aircrafts were the subject of [13], who treated actuator fault diagnosis and [14] who developed multiple model adaptive estimation for sensor and actuator faults. Extended Kalman filtering techniques were combined with diagnosis to obtain fault-tolerant control in [15] who also demonstrated detection of faults and degraded performance of actuators using both simulated and real flight data. The airspeed sensor problem was not dealt with in this literature. A general structural analysis was conducted by [16] for a non-linear aircraft model, and structural detectability and isolability properties were determined. Classical diagnostic techniques was shown, but on simulated data. Specific faults and failure modes have also attracted considerable attention, performance monitoring and detection of oscillatory behavior was treated in [17]. Research on the airspeed sensor problem using multiple sensors have been treated in [18] and [19] who analyzed performance of linear time-invariant fault detection methods applied on parallel airspeed sensors, but more general results on airspeed sensor fault diagnosis have been sparse. Larger manned aircraft use heating of airspeed sensors to prevent icing but this is not always enough to avoid problems. The final report on the Air France AF447 accident [20] states that the pilots misinterpretation of faulty airspeed measurements

was the leading cause of the incident. This has caused a lot of visibility in the flight control system community towards air speed sensor faults and alternatives to the use of classical voting principles as sole means of fault diagnosis.

The present research started well in advance of the AF447 accident because air speed sensor signal faults and artifacts have long been an issue on small unmanned aircraft. The paper focus on the airspeed sensor FDI problem using non-linear analytical redundancies. Early results [21] showed that fault detection for clogging of a pitot tube was feasible but used a simplified setup where wind was assumed known and propulsion dynamics was known a priori. This paper presents a complete solution to the airspeed sensor detection problem where wind speed and propulsion dynamics are unknown. An extended Kalman filter technique is adopted to the problem at hand to estimate the wind velocity vector while flying and propulsion system parameters and airspeed are estimated by a dedicated nonlinear observer. The test statistics obtained by generalized likelihood change detection is scrutinized using multiple flight experiments to obtain parameters for the distribution of the test statistics, both in normal and faulty conditions. It is shown how the parameters of estimated test statistics can be used to determine thresholds for detection that guarantee very low probability of false alarms while ensuring adequate detection capability. A special methodology is developed to avoid false diagnosis for return to normal, which is a problem for an aircraft that experience uncontrolled nonlinear behavior at the boundary of stability or in rapid maneuvers. It is discussed how the diagnostic scheme could be implemented as part of on-board avionics but also, as an added benefit, be implemented as part of a mission supervisor on a ground station based on aircraft telemetry. If a fault is detected an alarm could be raised to let the operator take appropriate action to bring it down safely.

The paper is structured as follows. Following a brief problem statement and presentation of selected parts of equations of motion and propulsion dynamics, a set of residuals relations are derived. To cope with parameter uncertainty and variability, a non-linear high-gain observer is used to estimate the force balance on the aircraft to get the expected speed from thrust relations of the propeller. Wind speed is estimated by an EKF and added to ground speed from an onboard GPS unit to get a airspeed estimate. Robust residual generators are implemented and validated using recorded flight data.

II. BANSHEE UAV SYSTEM

Research on fault diagnosis is often based primarily on simulation studies, but the randomness caused by practical conditions for unmanned aircrafts, including change of pay-load, pre-flight trimming and control surface adjustments, cause flight conditions to vary more than commonly captured in simulations. The results in this paper are based on data records from a large number of UAV flights under, most under what are considered normal conditions, some are cases of real faults that led to incidents with loss of aircraft.

This section gives a short introduction to the UAV from which data originate. The aircraft is a Banshee drone from Meggitt Defence Systems (UK), widely used for target practise in several countries [22].

The Banshee UAV is a delta wing aircraft propelled by a rear mounted engine. The thrust is delivered by a 2 bladed propeller. It is launched from a catapult system (see Fig. 1) and lands by parachute. It is not equipped with a landing gear.

Fig. 1. A Banshee UAV ready for launch. *Photo: Danish Forces Joint UAV Team*

The aircraft has an avionics with an autopilot system that is operated via telemetry from ground. A path to follow is defined by a number of waypoints and speed to be followed between waypoints. It is technically possible to fly the drone manually and throttle command to control speed is feasible, but when out of sight, remote command for attitude control is difficult if not impossible.

A. Banshee Sensors and Actuators

In the configuration used for the tests in this paper, the Banshee UAV was equipped with actuators and sensors, listed in Table I, together with the associated signals.

The autopilot on this drone has a non-redundant architecture and depends solely on individual sensor input to function correctly. Only one sensor is present for each physical variable and possible sensor artifacts or faults ripple directly to the avionics. Faults on actuators limit the envelope within which stable flight is possible. Calculating the flight envelope through a linear matrix inequality problem formulation was pursued in [23] and [15]. With closed loop speed control along a track and attitude controller parameters being scaled by airspeed, erroneous airspeed input will limit the flight envelope, in particular when conducting sharp turns or other maneuvers. Remedial actions on this UAV in its standard configuration are possible only via telemetry from ground. If an airspeed sensor issue is detected, the autopilot can be switched to a mode without closed loop speed control; a less agile attitude control can be selected to obtain better robust stability; the ultimate fail-safe reaction is to stop the engine and release the parachute. Activation of remedial action via ground station command requires that the diagnostic result is available and presented to the operator timely enough to intervene. Time to detect, fault isolation probability and false alarm probability are essential quality parameters that will be design drivers in the sequel.

TABLE I
LIST OF COMMANDS AND MEASURED OUTPUT

Symbol	Unit	Explanation
h_p	m	Altitude measured by pressure
v_{pitot}	m/s	Airspeed measured by pitot tube
$\lambda_{lat}, \lambda_{lon}$	deg	Latitude and longitude measured by GPS
v_{gps}, ψ_{gps}	m/s, deg	Speed and course over ground from GPS
p_i, q_i, r_i	deg/s	Roll rate, pitch rate, and yaw rate measured by IMU
a_x, a_y, a_z	m/s^2	Body axis accelerations measured by IMU
n	s^{-1}	Engine revolutions
δ_T	%	Throttle
δ_a	deg	Aileron deflection
δ_e	deg	Elevator deflection

III. THRUST DELIVERED BY THE PROPELLER

The Banshee is propelled by a rear mounted combustion engine with a 2 bladed wood propeller. The thrust developed by this engine F_T is given by k_T, a non-dimensional thrust coefficient, made dimensional by

$$F_T = k_T \varrho n^2 d_p^4, \quad (1)$$

where propeller diameter is d_p, shaft speed n, and ϱ the air density. Wind tunnel tests (see [24]) of propellers of the type used reveals that the thrust coefficient is approximately linear with the advancement ratio $J = \frac{v}{nd_p}$, where v is inflow velocity to the propeller. The thrust coefficient and NACA data are plotted in Fig. 2. In nominal flight J is in the range
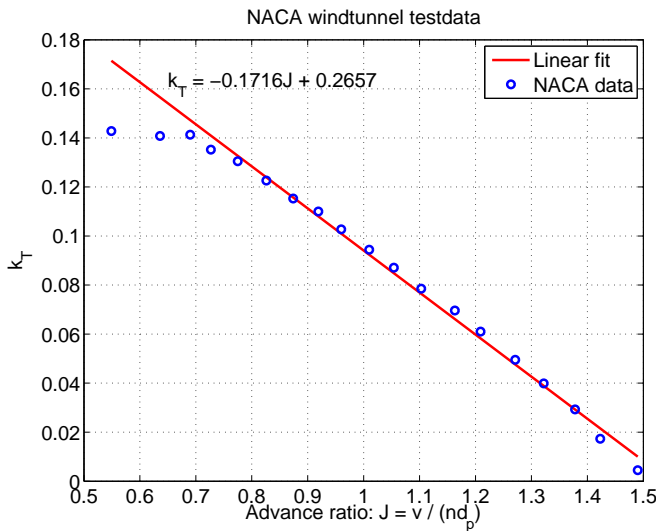

Fig. 2. NACA wind tunnel test of two bladed propeller. Non-dimensional thrust k_T versus advancement ratio J.

0.9 to 1.1.

Propellers are usually characterized by their diameter d_p and pitch P_p. These values can be combined to a non-dimensional pitch defined by $P' = \frac{P_p}{d_p}$. The following scaling for the thrust coefficient was proposed by [25]

$$k_T(J) \simeq k_{T,\text{ref}}(J - (P' - P'_{\text{ref}})), \quad (2)$$

where $k_{T,\text{ref}}$ and P'_{ref} are the thrust coefficient and non-dimensional pitch of the reference signal, respectively. The reference signals originates from different propellers tested in [24]. The 26×32 propeller used on the Banshee has

P' equal to that of one of the tested propellers and the characteristics of this propeller are used.

Calculating dimensional lift and drag on a propeller, it was shown in [26] that thrust is related to advance speed v and propeller angular speed n by the bi-linear expression

$$F_T = T_{nn}n^2 + T_{nv}nv, \quad (3)$$

which was shown equivalent to a linear approximation to non-dimensional thrust

$$k_T = k_{T0} + k_{T1}J, \quad (4)$$

where dimensional and non-dimensional parameters are related as $T_{nn} = k_{T0}\varrho d_p^4$ and $T_{nv} = k_{T1}\varrho d_p^3$.

IV. POSSIBILITIES FOR DIAGNOSIS

When three measurements of a compatible quantity V_k are available, the classical *Voting Scheme* technique for fault isolation calculates the three differences $V_i - V_j$, $(i,j) \in [1,2,3], i \neq j$. The measurements available on the aircraft provide, at a first glance, three obvious redundancies, the airspeed measurement v_{pitot}, velocity measured by GPS and compensated for wind $v_{gps2air}$, and the expected velocity v_{thrust} obtained at a known shaft speed of the engine. This gives rise to the parity relations shown in Table II, which were also used in [21]. A "1" in Table II means the residual

TABLE II
MEASUREMENTS AND VOTING SCHEME RESIDUALS.

Residual	v_{pitot}	$v_{gps2air}$	v_{thrust}
R_1	1	1	0
R_2	1	0	1
R_3	0	1	1

is affected by the measurement, and since all three columns have different column signatures, faults on each of the three measurements could appear as easily isolable. The catch in this argument is that $v_{gps2air}$ and v_{thrust} are not independent of v_{pitot}: $v_{gps2air}$ need an estimate of wind velocity, which requires the airspeed through v_{pitot}; v_{thrust} is dependent on propulsion parameters, trim and loading conditions, and parameter adaptation also needs v_{pitot}. These apparent difficulties are analyzed and overcome in the sequel of the paper, and it is shown how a combination of estimation, adaptation, statistical change detection and dedicated hypothesis testing together can solve the robust fault isolation problem.

V. RESIDUAL R_1 FROM GROUND SPEED AND ESTIMATED WIND

An estimate of the wind velocity vector is needed to create residual R_1 comparing airspeed readings: One from the pitot tube system, the other being the sum of GPS measured ground speed plus estimated wind vector. In [27] such an estimate was developed with the purpose of calibrating the airspeed sensor of a small UAV. Since this estimation algorithm is simple and is shown to work well for an aircraft with the same instrumentation as the Banshee, it is adopted here albeit with a different end purpose, namely fault detection.

The aircrafts velocity relative to air v_{rel} is related to the ground speed vector v_g according to the following vector sum: $v_g = v_{rel} + v_w$. The wind velocity vector is defined such that it points in the direction the wind blow. The size of the airspeed can then be formulated using the standard cosine rule for triangles

$$v_{rel}^2 = v_w^2 + v_g^2 - 2v_g v_w \cos(\psi_w - \psi_g), \quad (5)$$

where the wind direction is ψ_w and the heading of the aircraft is denoted ψ_g. The relationship is illustrated in Figure 3.
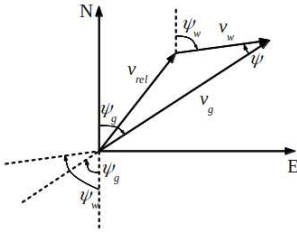

Fig. 3.   Relationship between ground speed, airspeed and wind speed.

The pitot tube basically measures the dynamic pressure of the wind flow based on pressure readings from a tube pointing in the aircrafts forward direction and static vent on the fuselage. Therefore, the pitot tube reading is a measure of the forward speed u in the body frame (Appendix A). To take differences between the measurement from the pitot tube and the aircraft's real speed due to attack angle, α, and sideslip, β, into account, a factor between the two values also needs to be estimated,

$$v_{pitot} = \cos(\alpha)\cos(\beta)v_{rel} \simeq a v_{rel}. \quad (6)$$

An EKF was used in [27] to estimate the wind vector and a scaling factor. The dynamic pressure was available as a measurement on the aircraft and was therefore used in the measurement equation. For the Banshee the airspeed is given as a velocity and (5) is used directly as measurement equation.

The state vector of the EKF is given by $x = [v_w, \psi_w, a]^T$ and states are modelled as random-walk processes. This gives the state transition

$$x_k = I x_{k-1} + \nu_k, \quad (7)$$

with $\nu_k \sim \mathcal{N}(0, Q_k)$. The pitot tube measurement can be estimated from the states by the following observation equation based on (5)

$$\hat{h}(x) = a\sqrt{v_w^2 + v_g^2 - 2v_g v_w \cos(\psi_w - \psi_g)}. \quad (8)$$

Since the ground speed and heading is estimated by the onboard GPS receiver this observation equation can be re-formulated as

$$\hat{h}(x) = a\sqrt{v_w^2 + v_{gps}^2 - 2v_{gps}v_w \cos(\psi_w - \psi_{gps})}. \quad (9)$$

This leads to the following Jacobian

$$H = \begin{bmatrix} \dfrac{a(2v_w - 2v_{gps}\cos(\psi_w - \psi_{gps}))}{2\sqrt{v_w^2 + v_{gps}^2 - 2v_{gps}v_w \cos(\psi_w - \psi_{gps})}} \\[2mm] \dfrac{a(2v_w v_{gps}\sin(\psi_w - \psi_{gps}))}{2\sqrt{v_w^2 + v_{gps}^2 - 2v_{gps}v_w \cos(\psi_w - \psi_{gps})}} \\[2mm] \sqrt{v_w^2 + v_{gps}^2 - 2v_{gps}v_w \cos(\psi_w - \psi_{gps})} \end{bmatrix}^T. \quad (10)$$

The standard EKF algorithm (see eg. [28]) is utilized using the above equations. This gives the following time update step

$$\hat{x}_{k|k-1} = \hat{x}_{k-1|k-1} \quad (11)$$
$$P_{k|k-1} = P_{k-1|k-1} + Q_k, \quad (12)$$

and the measurement update is

$$\tilde{y}_k = z_k - \hat{h}(x_{k|k-1}) \quad (13)$$
$$K_k = P_{k|k-1}H_k^T (H_k P_{k|k-1}H_k^T + R_{k-1})^{-1} \quad (14)$$
$$\hat{x}_{k|k} = \hat{x}_{k|k-1} + K_k \tilde{y}_k \quad (15)$$
$$P_{k|k} = (I - K_k H_k) P_{k|k-1}. \quad (16)$$

The covariances Q_k and R_k are found from analysis of segments of data during level flight. Alternatively they could be estimated in the filter following methods suggested for linear systems in Ljung's innovations filter [3] and extended to nonlinear systems in [4].

A typical development of the states for a flight is shown in Fig. 4. The wind was measured on ground to be 6.8 m/s
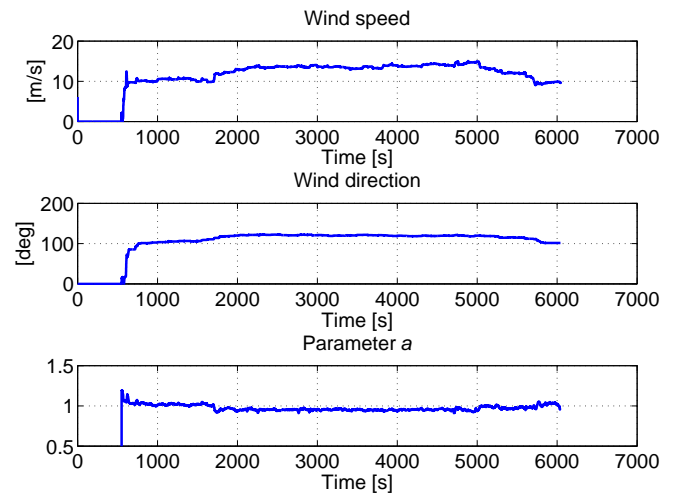

Fig. 4.   Estimates of wind parameters during a flight at altitude up to 1500 m.

at $80°$, however, since the aircraft was flying at heights up to
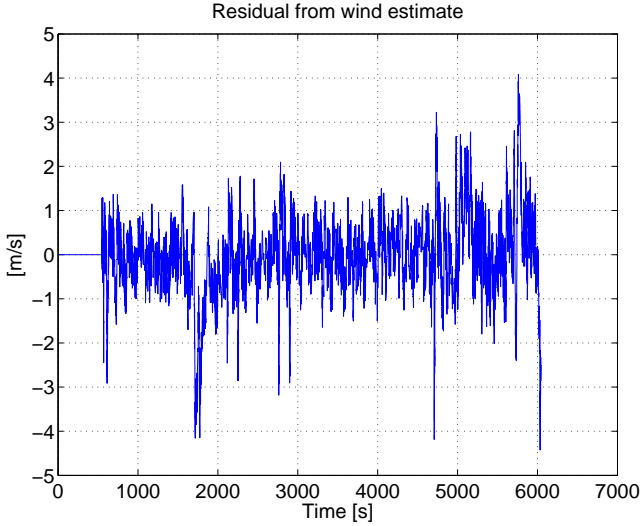
Fig. 5. Time development of the innovation of the EKF for same flight as in Fig. 4.

1500 m the ground measured velocity was not representative. The innovation of the filter is the difference between the measured air speed component in the x direction and the x-component estimated from ground speed plus the contribution from wind. This innovation, Eq. (13), is used as residual R_1 from Table II. With actual variables inserted

$$R_1 = v_{pitot} - \hat{a}\sqrt{\hat{v}_w^2 + v_{gps}^2 - 2v_{gps}\hat{v}_w \cos(\hat{\psi}_w - \psi_{gps})}. \tag{17}$$

The time-history of R_1 is plotted in Fig. 5 for the same flight as was illustrated in Fig 4.

VI. RESIDUAL R_2 FROM ADAPTIVE OBSERVER BASED ON PROPELLER SPEED

The second residual R_2 in Table II is based on thrust delivered by the engine and an associated estimate of airspeed. This estimate is available through exploiting the dynamics, in component form

$$m\dot{u} = m(rv - qw) + F_{Ax} - mg\sin(\theta) + F_T, \tag{18}$$
$$m\dot{v} = m(pw - ru) + F_{Ay} + mg\cos(\theta)\sin(\phi), \tag{19}$$
$$m\dot{w} = m(qu - pv) + F_{Az} + mg\cos(\theta)\cos(\phi). \tag{20}$$

The aircraft's motion is described by its linear and angular velocities, $\boldsymbol{v}_b = [u, v, w]^{\mathrm{T}}$ and $\boldsymbol{\omega} = [p, q, r]^{\mathrm{T}}$, in the body frame, the euler angles ϕ, θ, ψ. The aerodynamic forces are F_{Ax}, F_{Ay}, F_{Az} and F_T is the thrust forces derived in section III.

The velocities are related to the relative airspeed, v_{rel}, as

$$u = v_{rel}\cos(\alpha)\cos(\beta), \tag{21}$$
$$v = v_{rel}\sin(\beta), \tag{22}$$
$$w = v_{rel}\sin(\alpha)\cos(\beta), \tag{23}$$
$$v_{rel} = \sqrt{u^2 + v^2 + w^2}. \tag{24}$$

As the aircrafts fly with wings levelled most of time the magnitudes of v and w generally are small so when calibrated,

the pitot tube provides a reading of the forward airspeed, hence

$$u = v_{pitot}, \tag{25}$$

and the velocity can be approximately described using only the u term in (18). Since the aerodynamic force F_{Ax} is unknown, this term has to be estimated by the observer. This is done by adding an adaptation scheme to the observer. It is customary to describe forces in terms of non-dimensional parameters, for reasons of scaling, and it provides some numerical advantage to use this representation in the adaptive observer. The aerodynamic force in the x direction is,

$$F_{Ax} = \bar{q}SC_x = \tfrac{1}{2}\varrho v_{rel}^2 SC_x, \tag{26}$$

with $\bar{q}$ being the dynamic pressure and S the surface area of the aircraft. C_x is composed by lift C_L and drag C_D as (from [29])

$$C_x = C_L \sin(\alpha) - C_D \cos(\alpha). \tag{27}$$

Based on this the following model for F_{Ax} is suggested. It contains two unknown parameters $\boldsymbol{\Theta} = [\Theta_{uu}, \Theta_{uu\alpha}]^{\mathrm{T}}$ to be estimated.

$$F_{Ax} = \tfrac{1}{2}\varrho Su^2 (\Theta_{uu} + \Theta_{uu\alpha}\alpha) \tag{28}$$

This model depends on α which is not desirable because most low cost UAV's does not have a direct measurement of this value. Instead a model only containing the velocity dependent part is suggested. and if α is not available, the following one-parameter approximation is used

$$F_{Ax} = \tfrac{1}{2}\varrho Su^2 \Theta_{uu}. \tag{29}$$

Both force models (28) and (29) was tested on real data to see which one gives the best estimates for the purpose of fault diagnosis. The Banshee does not have a vane measuring α but an estimate is available from the autopilot. Using this estimate in getting F_{Ax} from (28) does not give any additional performance compared to (29). This could be because the α estimate is inaccurate or the tested flight patterns does not exceed the α dependence enough. Therefore the fault diagnosis is done using (29) for F_{Ax}. Results from using the two estimates are given in section VI-A.

The derivation is continued for the two parameter model (28), but the results are valid also for the one-parameter model by setting $\Theta_{uu\alpha} = 0$ in the following. The model for F_{Ax} can be written as

$$F_{Ax} = m(F_1(u,t)\Theta_{uu} + F_2(u,t)\Theta_{uu\alpha}), \tag{30}$$

where the $F_1(u,t)$ and $F_2(u,t)$ are defined as

$$F_1(u,t) = \frac{\varrho Su^2}{2m} \quad , \quad F_2(u,t) = \frac{\varrho Su^2\alpha}{2m}, \tag{31}$$

and m is pre-multiplied on the right hand side of (30) for later convenience.

From the system equations (18), the following nonlinear, adaptive observer is a natural choice for estimation of u. Let $\hat{u}$ denote the estimate of u and let L be the gain the observer uses to update the estimate of linear acceleration from the output innovation $u - \hat{u}$. The measurement of u is obtained

from the pitot tube measured air speed v_{pitot} according to (25). Hence

$$\dot{\hat{u}} = -g\sin(\theta) + \frac{T_{nn}n^2 + T_{nu}n\hat{u}}{m} \tag{32}$$
$$+ \; F_1(\hat{u},t)\hat{\Theta}_{uu} + F_2(\hat{u},t)\hat{\Theta}_{uu\alpha} + L(v_{pitot} - \hat{u}).$$

The pitch angle θ is estimate by the onboard inertial measurement unit.

The unknown parameters are estimated using a standard adaptive observer updating approach, (see e.g [2])

$$\begin{bmatrix} \dot{\hat{\Theta}}_{uu} \\ \dot{\hat{\Theta}}_{uu\alpha} \end{bmatrix} = \begin{bmatrix} F_1(\hat{u},t) \\ F_2(\hat{u},t) \end{bmatrix} (v_{pitot} - \hat{u}). \tag{33}$$

The estimation is initialized with values found during previous fault-free flights. This ensures a fast transient period.

The extended state and parameter vector $\boldsymbol{x}$ of the observer is then

$$\dot{\hat{\boldsymbol{x}}} = \begin{bmatrix} \dot{\hat{u}} \\ \dot{\hat{\Theta}}_{uu} \\ \dot{\hat{\Theta}}_{uu\alpha} \end{bmatrix} = \begin{bmatrix} \dot{\hat{u}} \\ F_1(\hat{u},t)(v_{pitot} - \hat{u}) \\ F_2(\hat{u},t)(v_{pitot} - \hat{u}) \end{bmatrix}, \tag{34}$$

and with parameters Θ_{uu} and $\Theta_{uu\alpha}$ assumed unknown constants, the error dynamics is

$$\boldsymbol{f}(\tilde{\boldsymbol{x}}) = \dot{\tilde{\boldsymbol{x}}} = \dot{\boldsymbol{x}} - \dot{\hat{\boldsymbol{x}}} = \begin{bmatrix} \dot{\tilde{u}} \\ \dot{\tilde{\Theta}}_{uu} \\ \dot{\tilde{\Theta}}_{uu\alpha} \end{bmatrix} = \begin{bmatrix} \dot{\tilde{u}} \\ -F_1(\hat{u},t)\tilde{u} \\ -F_2(\hat{u},t)\tilde{u} \end{bmatrix}. \tag{35}$$

For the diagnosis the error $\tilde{u}$ of the observer expresses exactly what residual R_2 from Table II contains, a comparison between airspeed measured by the pitot tube u and an estimate $\hat{u}$ based on the thrust force delivered by the engine.

The observer gain L must be chosen high enough to ensure that the observer is uniformly asymptotically stable. A stability proof is provided in Appendix B. In order for the observer to have good performance with respect to the fault diagnosis it is important to choose a gain value that allows sufficient deviation of the error value. Too high a gain could give an observer that could track measurements, thereby creating fairly weak detectability of a sensor fault, but also making estimated parameters change so much that the parameter change itself should trigger an alarm. When deciding whether to detect a change from the observer's innovation, or from the estimated parameters, it is worth noting that the innovation is driving the parameter updating, and a change (fault) in the generating process or sensor is therefore first visible in the innovation. It is hence a natural choice to use the innovation for change detection when rapid detection is of prime concern.

Using model parameter adaptation together with residual generation based on the filter innovation raises questions about how and when the estimator itself need be updated to changed conditions. Some techniques to combine change detection with change in adaptation gains was treated in [30], who demonstrated the combined technique on detection of multiple changes, but the problem is an area of continued research [31]. Aiming at fast online diagnosis, this paper will halt adaptation when the output (test statistics) from a change detector exceeds specified values, which are lower than the

chosen alarm threshold, and a special hypothesis test will be developed to prevent false resetting of alarms.

A. Observer performance

The performance of the adaptive observer was tested using recorded data from 18 flights with the Banshee UAV. Fig. 6
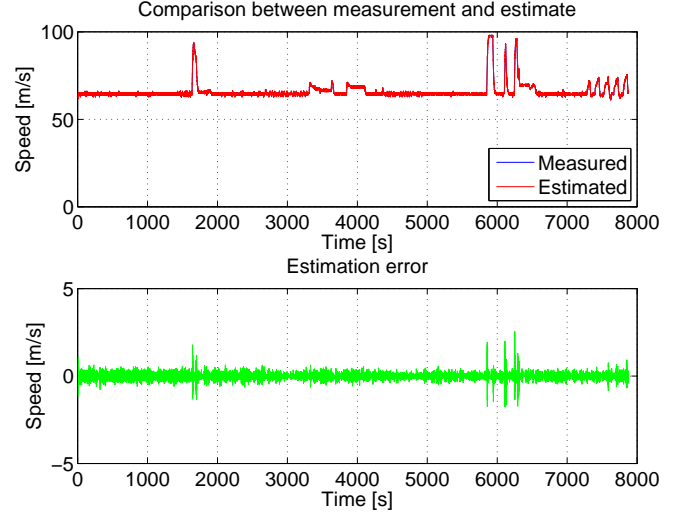

Fig. 6. Observer performance and choice of model.

shows the estimated speed of the vehicle compared with measured airspeed in the upper part of the plot and the observer's innovation in the lower plot. It is apparent that the observer is stable and the standard deviation of the error, for the given flight, is 0.23 m/s, which is satisfactory compared to the 0.5 m/s present on the airspeed measurement when we do not wish too high filtering (low bandwidth) in the adaptive observer as this would delay fault detection.

The unknown parameters Θ behave, over time, as seen on Fig. 7. Fig. 7 also shows that $\hat{\Theta}_{uu\alpha}$ drifts in value. This has no
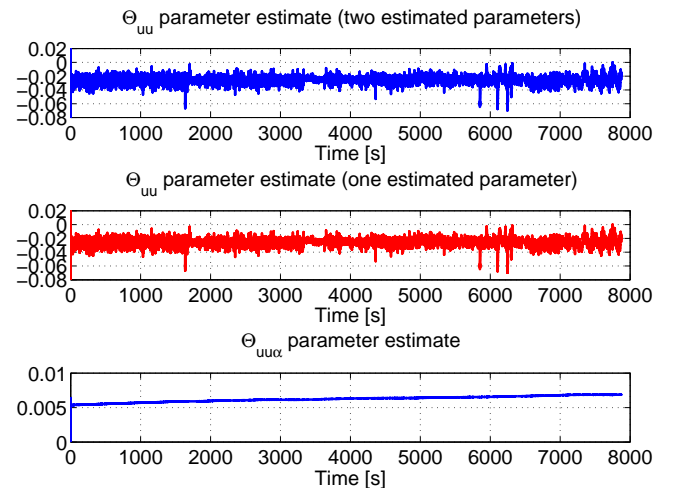

Fig. 7. Parameter development during estimation. The blue plots are the two parameter observer which has $\sigma_{\tilde{u}} = 0.22\text{ m/s}$ and the red curve represents the one parameter setup which has $\sigma_{\tilde{u}} = 0.23\text{ m/s}$.

effect on the residual since its value is very small compared

to $\hat{\Theta}_{uu}$ and the reasons could include some change in trim as fuel is consumed during the flight. Another reason for the drift could be that the angle of attack, α, does not vary much and sufficient excitation is not present to identify $\hat{\Theta}_{uu\alpha}$ without drift. The one-parameter formulation (29) avoids this issue, it is simpler and it's innovation has very similar properties. The two parameter observers standard deviation error is 0.22 m/s compared to 0.23 m/s for the one parameter setup. The parameter estimate using the one-parameter adaptation scheme is shown in the middle plot of Fig. 7. The observer in the one-parameter version

$$\dot{\boldsymbol{x}} = \begin{bmatrix} \dot{\hat{u}} \\ \dot{\hat{\Theta}}_{uu} \end{bmatrix} \tag{36}$$

$$= \begin{bmatrix} -g\sin(\theta) + \dfrac{T_{nn}n^2 + T_{nu}n\hat{u}}{m} \\ +F_1(\hat{u},t)\hat{\Theta}_{uu} + L(v_{pitot} - \hat{u}) \\ F_1(\hat{u},t)(v_{pitot} - \hat{u}) \end{bmatrix},$$

and residual R_2, which equals the observer innovation, $\tilde{u} = u - \hat{u}$, reads

$$R_2 = v_{pitot} + \tag{37}$$
$$\left(\int g\sin(\theta) - \frac{T_{nn}n^2 + T_{nu}n\hat{u}}{m} - F_1(\hat{u},t)\hat{\Theta}_{uu} dt \right)$$
$$- L(v_{pitot} - \hat{u}).$$

VII. RESIDUAL R_3 FROM COMPARISON OF VELOCITY ESTIMATES

Following the voting scheme described in Table II the third residual is the difference between the two estimates of airspeed. Since both $v_{gps2air}$ and v_{thrust} relies on the airspeed measurement in their estimation procedures, it is impossible achieve independence of v_{pitot}. However, since the purpose of R_3 is to ensure isolability of the airspeed measurement fault, its value is only required when R_1 and/or R_2 indicate an alarm. With

$$R_3 = v_{gps2air} - v_{thrust} \tag{38}$$
$$= \hat{a}\sqrt{\hat{v}_w^2 + v_{gps}^2 - 2v_{gps}\hat{v}_w\cos(\hat{\psi}_w - \psi_{gps})} + g\sin(\theta)$$
$$- \frac{T_{nn}n^2 + T_{nu}n\hat{u}}{m} - F_1(\hat{u},t)\hat{\Theta}_{uu} - L(v_{pitot} - \hat{u}).$$

and setting adaptation on hold when a fault is detected, R_3 can be used for isolation. If an airspeed fault is detected, v_{pitot} can not re-enter in calculations that estimate $v_{gps2air}$ and v_{thrust}. These estimates will therefore after a while become increasingly uncertain, which in turns affects R_3. However, as long as R_3's value is reliable up to and shortly after detection, it serves the purpose.

VIII. CHANGE DETECTION

As in [21] fault detection is achieved by detecting changes to the residual signals (17) and (37). Generalized Likelihood Ratio Tests (GLRT) are used to distinguish between to possible hypothesis about the residual signals.

$$\begin{aligned} \mathcal{H}_0 : x[n] &= w[n] \\ \mathcal{H}_1 : x[n] &= A + w[n]. \end{aligned} \tag{39}$$

The $\mathcal{H}_0$ hypothesis is that only the expected noise is present on the signal and the alternative $\mathcal{H}_1$ hypothesis states that the signal has been offset from 0 by a value of A. If this is the case there must be a significant difference between the measurement and the model and hence a fault is present. In Fig. 8 the histogram and autocorrelation of the residual
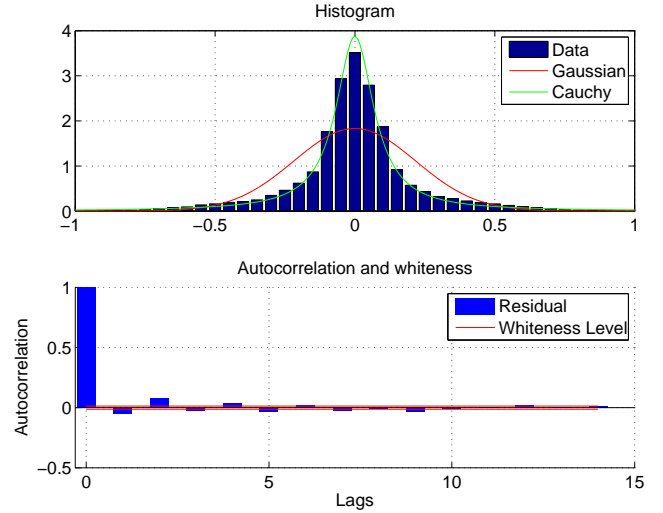

Fig. 8. Residual from wind estimating EKF characteristics.

from the wind estimator is shown. The residual has been pre-whitened and is uncorrelated with past samples as seen in the figure. The histogram shows that as in [21] the noise on the residual follows a Cauchy distribution with a general form of

$$p(x; x_o, \beta) = \frac{1}{\pi} \frac{\beta}{(x - x_o)^2 + \beta^2}. \tag{40}$$

The GLRT is based on the likelihood ratio between the probability of the two hypotheses given a window of data

$$L_G(\boldsymbol{x}) = \frac{p\left(\boldsymbol{x}; \hat{\boldsymbol{\Theta}}_1\right)}{p\left(\boldsymbol{x}; \hat{\boldsymbol{\Theta}}_0\right)} > \gamma. \tag{41}$$

Here $\hat{\boldsymbol{\Theta}}_1$ is the Maximum Likelihood Estimate (MLE) of the parameters given $\mathcal{H}_1$ and $\hat{\boldsymbol{\Theta}}_0$ for the null-hypothesis. If the ratio is larger than a certain threshold γ the hypothesis $\mathcal{H}_1$ is decided. The two parameters of (40) are the half-width half-maximum scaling, β, and the offset x_o, respectively. Using this equation the GLRT test statistics become

$$L_G(\boldsymbol{x}) = \frac{\prod_{i=1}^{N} p\left(x_i; \hat{x}_o, \hat{\beta}\right)}{\prod_{i=1}^{N} p\left(x_i; 0, \hat{\beta}\right)} > \gamma. \tag{42}$$

The MLEs of $\hat{\beta}$ and $\hat{x}_o$ are found by fitting the data to equation 40. The window size N is chosen empirically. In [21] the threshold for the detector was found by assuming the performance could be calculated using a χ^2 distribution for the detectors, according to the classical theory [32], [33]. Dong et. al [34] introduced a robust scheme for online fault detection of additive faults on an aircraft when identification errors exist in the model on which FDI is based. Other data driven

approaches utilize observations on real data to characterize the distributions of test statistics that are found to differ significantly from the theoretical χ^2 in real applications, see [35] and [36]. This paper follows the latter approach and instead of assuming a χ^2 determined threshold, the distribution of the test statistics, ie the L_G signal, is determined for a large sample of data known to have no observed faults. This makes it possible to provide a reliable estimate of the P_{FA} (probability of false alarms) under $\mathcal{H}_0$. The idea to design tests based on P_{FA} under $\mathcal{H}_0$ was investigated in [37] for a CUSUM test and in [38] for CUSUM and GLRT with χ^2 test statistics.
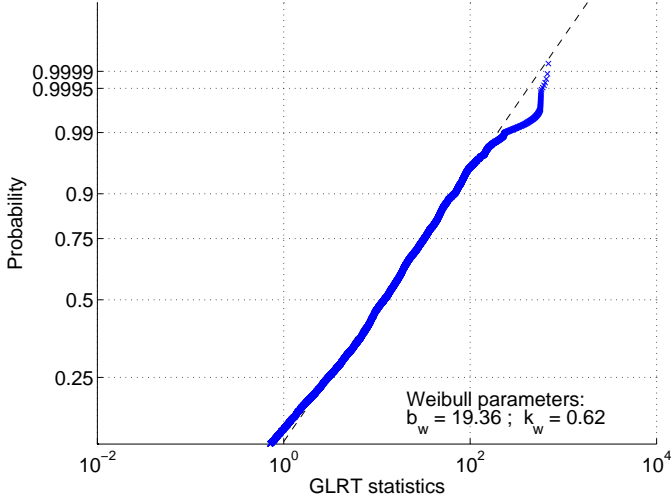

Fig. 9. Probability plots of the GLRT output for the fault free part of a flight.

Fig. 9 shows the GLRT test statistics for a part of a flight without presence of faults. The data are found to be best fitted using a Weibull distribution

$$P(x; b_w, k_w) = 1 - \exp\left(-\left(\frac{x}{b_w}\right)^{k_w}\right). \qquad (43)$$

Estimating the scale parameter b_w and shape parameter k_w is straight forward using an MLE or moment estimator method. The threshold γ that will give a desired low false alarm probability is obtained from the estimate of the distribution. The MLE estimates of the parameters for 18 flights are shown in Fig. 10.

Some flights have a more noisy residual and therefore also a more noisy GLRT response. This is probably because this flight is done at higher altitude and on a day with more wind gusts, which doesn't fit well with the constant wind model used in the EKF. The fitted Weibull distribution is used to set the detector threshold. This is done by looking at the right tail distribution $Q(x; b_w, k_w) = 1 - P(x; b_w, k_w)$ to find the probability of exceeding a chosen threshold.

Due to differences the athmospheric conditions as well as differences between aircraft and flight-pattern there is a variation on the distribution parameters. In Fig. 10 MLEs for the Weibull parameters for 18 different test flights show that the shape parameter k_w is fairly constant among these flights. The scale parameter b_w however, varies with the conditions
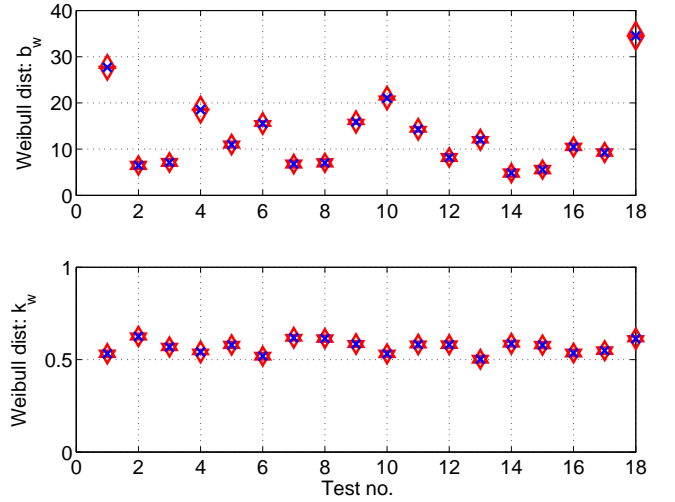

Fig. 10. Maximum likelihood estimates of Weibull parameters for different flights together with 99% confidence boundaries (red arrows).

met during the individual flights. By scaling test statistic data with the estimates of b_w, it is hence possible to get a quite homogeneous set of test statistics data from which a suitable threshold can be found. The right tail probability $Q(x; b_w, k_w) = 1 - P(x; b_w, k_w)$ gives the probability of exceeding a chosen threshold. The 0.9999 level in the probability plots give $P_{FA} = 0.0001$.

$$P_{FA} = Q(\gamma; b_w, k_w) \Rightarrow \gamma = b_w \left(-\ln\left(P_{FA}\right)\right)^{\frac{1}{k_w}}. \qquad (44)$$

With sampling time $T_S \simeq 0.1s$, choosing $\gamma_1 = 3000$ will give a false alarm probability of 0.003% per hour of flight for the data from Fig 10 ($b_w = 19$ and $k_w = 0.6$). This might even be a conservative choice since data does not follow the Weibull distribution in the high end of the probability plot in Fig. 9.

The threshold to be selected for a chosen false alarm rate is clearly higher in conditions with high levels of wind turbulence. An alternative to a fixed threshold could be development of an adaptive threshold. This has been done for CUSUM-like tests and for χ^2 type test statistics in [39]. Similar results are not available for a GLRT and Weibull distributed test statistics.

The residual from (35) is treated in a similar way to find parameters for a suitable GLRT detector and a threshold of $\gamma_2 = 100$ is found to give an acceptably low false alarm rate, below $0.003/\text{h}$ for the worst case level of disturbances. If a less conservative calculation was made based on the mean of the Weibull parameters a threshold of $\gamma_i/2$ would give a false alarm rate of around $0.0004/\text{h}$. The conservative choice of threshold is used because of the large variation between the noise of the different flights makes it too risky to provide with the lower bound.

Since both residual R_1 and R_2 are based on estimators that uses v_{pitot} in their error values, it is important to stop estimation when a fault on v_{pitot} is detected. Each of the estimators are stopped when its corresponding GLRT output reaches a certain fraction of the alarm threshold, a value of $\gamma_i/2$ was used here. Choosing a lower boundary for this than the alarm threshold has two important advantages. First R_3, which is based on the difference of the two estimates,

is independent of v_{pitot} some samples before an alarm is triggered such that isolation is possible. Second, the chance of adapting to a faulty state is lower because adaption is stopped sooner after the fault.

A. Detection Probability

Detection probability P_D is much more difficult to assess than the false alarm probability P_{FA} due to the sparsity of data where faults are present, the $\mathcal{H}_1$ cases. A single recorded case of a pitot sensor fault is available but the duration of the fault is fairly short, since the event caused the UAV to get into uncontrolled conditions that led to a crash. There is no *ground truth* available of when to declare the start of a $\mathcal{H}_1$ condition, so the statistical assessment of P_D that follows is fairly uncertain.

B. Test statistics for the $\mathcal{H}_1$ case

A portion of data for the faulty case is analyzed in this section. The data belongs to the part where the GLRT detectors chooses hypothesis $\mathcal{H}_1$. Even though the amount of data is small they could give an indication of detection probability given the thresholds chosen from the $\mathcal{H}_0$ data. The data is taken from the point where the fault is first deemed present on the data to three seconds before the first zero crossing of the residual. This slice of data covers the flight where the operator still would able to safe the aircraft and is therefore the most interesting for detection. Fig. 11 shows a probability
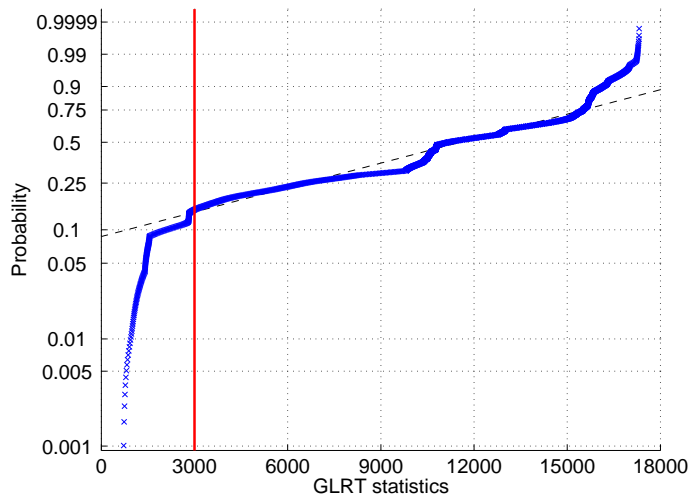

Fig. 11. Plot of the GLRT output in the $\mathcal{H}_1$ case for R_1. The red line indicates the threshold γ_1.

plot of the data in this $\mathcal{H}_1$ case for R_1. A Gumbel distribution is fitted to the data and shown in the plot. With the chosen threshold, and the chosen data segment, P_D is 85%. This is very satisfactory considering the noise level on the different measurements.

Another essential aspect is which effect the fault might on the flight envelope and derived from this on the operability and the survivability of the aircraft. Coverage, the probability of being able to detect and recover from a fault, was treated in [40], and fault masking in [41]. Methods to verify and test

for robust performance under different conditions of faults was the subject of [42].

The impact of the airspeed sensor fault is related to the level (magnitude) of faults that could be hidden below a threshold for the GLR tests. If the avionics and aircraft together have robust performance within this level, diagnostic performance could be considered satisfactory.

C. Detector performance

The detection algorithm is verified by adding a number of artificial faults to real data from flights with similar properties as shown in Fig. 10. In this way, the actual noise of the system is preserved. The simulated fault is added to the airspeed measurement $v^*_{pitot} = v_{pitot} + f$ and the faulty value v^*_{pitot} is passed on to the detection system. The following fault scenarios were tested. A stepwise fault

$$f = \begin{cases} f = 0 & t < T_f \\ f = A_s & t \geq T_f \end{cases}, \quad (45)$$

and ramp fault

$$f = \begin{cases} f = 0 & t < T_f \\ f = s_r t & t \in \left[T_f; T_f + \frac{A_r}{s_r}\right] \\ f = A_r & t > T_f + \frac{A_r}{s_r} \end{cases} \quad (46)$$

Faults below a certain magnitude will not be detected as these are considered within the limits of the normal noise and disturbances on the system. The lower limits of what is achievable to detect is reported in Table III. Residual R_1 has

TABLE III
LOWER LIMITS FOR DETECTION FOR R_1 AND R_2.

Residual	A_s	A_r	s_r
R_1	6.5 m/s	7.5 m/s	0.50
R_2	4.8 m/s	5.0 m/s	0.35

worse performance than R_2 because a relatively high threshold is needed on this residual to take wind gust into account. To raise the certainty of a fault before an alarm is triggered, both residuals should indicate a $\mathcal{H}_1$ condition before this is reported to the operator. The values determined for R_1 are hence those that determine the actual performance of the diagnosis system with fixed threshold. It is seen that a deviation in speed measurement of about 13% need be tolerable by the control system. This is reasonable for practical design.

The minimal time available to detect a fault is also important, however in the setup where the diagnosis system serves as an aid to the UAV operator the reaction time of this operator plays a major role. Practical experiences with airspeed faults for the Banshee drone indicate that the measurement error on the pitot tube builds up gradually over time as the fault progresses. This means that it takes some time before the fault reaches a level that is critical to the flight of the aircraft, but also that the detection time is longer. A sudden change in value will become critical sooner, but is also easier to detect. Practical experiences have shown that the time elapsed from the fault begins until control of the aircraft is lost is around 200 s. This observation is based on the loss of several drones, presumably caused by airspeed sensor faults, but only one incident was scrutinized in the detail reported here.

D. Real-time implementation

In order to run the diagnosis online, while flying, the system must be running fast enough to keep up with the telemetry datastream coming from the aircraft at 10 Hz-12 Hz. Since the system is intended to be running on ground and not onboard the aircraft standard PC hardware can be used. The EKF used for wind estimation is a straight forward implementation since the direct expressions for the derivatives are available. The non-linear observer representation must be discretized in order to run on the computer. This is done using a 4th order Runge Kutta method to approximate the differential equations. The heaviest process is generating test statistics used for the GLRT. Finding the MLE for the Cauchy distribution for a window of data is done by optimization. By using the MLE's from the previous data window as initialization parameters for the next data window, this is fast. Running the steps of the algorithm at the specified rate is therefore not an issue.

If the system should run onboard the aircraft it might be necessary to decrease systems load since limited processing power is available here. Also the data is available at a higher rate and thereby increasing the load of the algorithm. However since this is not the intended use of this diagnosis system this is not pursued any further.

E. Detection of real fault

Data from a real incident where the pitot tube gets clogged is used to test the behavior of the detection system. Velocities
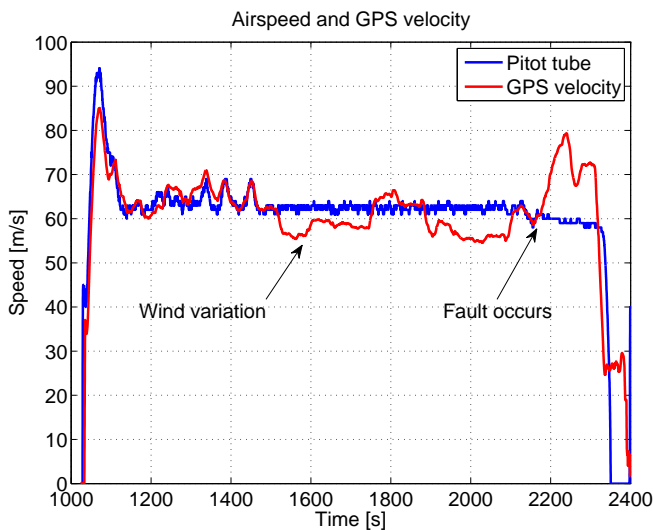

Fig. 12. Airspeed and GPS velocity for a flight where pitot tube clogging occurs.

measured by the pitot tube (airspeed) and the GPS (ground speed) are shown in Fig. 12. The figure shows that the two measurements follow each other relatively well until around 2140 s into the flight. There is some variation due to the wind and since the aircraft is flying in a square trajectory the effect of this is changing. The aircraft is controlled using airspeed which is why the pitot tube measurement is stable while the GPS velocity fluctuates. Around $t = 2140$ s into the flight a high increase in GPS velocity compared to airspeed is seen.

This is where the pitot tube measurement fails. Because the autopilot controls the aircraft as it was flying at its nominal speed a maneuver done around $t = 2333$ s exceeds the flight envelope and control of the aircraft is lost. The operator could have intervened and the aircraft saved had he been made aware that the pitot tube measurement was faulty.

The air data from the aforementioned flight was fed to the diagnosis system. The time development of three residuals
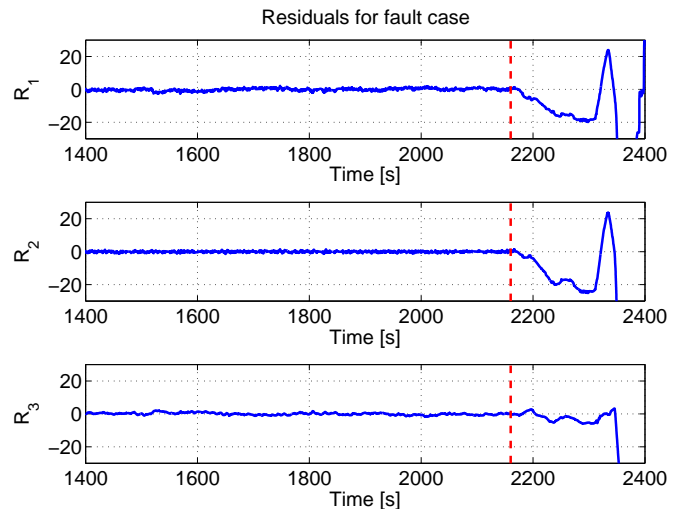

Fig. 13. All three residuals development for the faulty flight data. The vertical dashed line indicate the beginning of the fault.

described in Table. II is shown in Fig. 13 with an indication of the faults starting point. As expected a large response is seen on R_1 and R_2 which both triggers an alarm. A small variation is also observed in R_3. This is a consequence of the two airspeed estimators starting running open loop as the airspeed measurement is assessed being faulty. This means that after a while the estimates will diverge.

In Fig. 14 and 15 the resulting GLRT output is shown. Fig. 14 is residual R_1 originating by the wind estimating EKF. Note that the actual flight starts at $t = 1100$ s and the diagnosis is initialized a while after this to allow for estimated parameters to settle. With the chosen threshold detection is done at $t = 2204$ s, which is about 64 s from the first signs of the fault is seen. More importantly this is around 130 s before control over the aircraft is lost and therefore well within the operators reaction time.

In Fig. 15 the GLRT output and decision signal for R_2, the residual from the observer is shown. As seen the detection happens at $t = 2202$ s and is therefore in the same range as R_1 and well within reasonable time for the operator to react.

IX. HYPOTHESIS TESTING FOR RESET TO NORMAL

Resetting to normal could be essential for airspeed sensor faults if caused by icing. Testing for return to normal, the $\mathcal{H}_0$ condition is confirmed in a classical setting when performing a CUSUM sequential test where a hypothesis $\mathcal{H}_0 : R_i = \mu_0 + w(k); \quad \mu_0 \leq \mu_{test}$ where μ_{test} is a limit for declaring condition as normal. For GLRT, a test can be made that the test statistics remains below a specified threshold. These standard
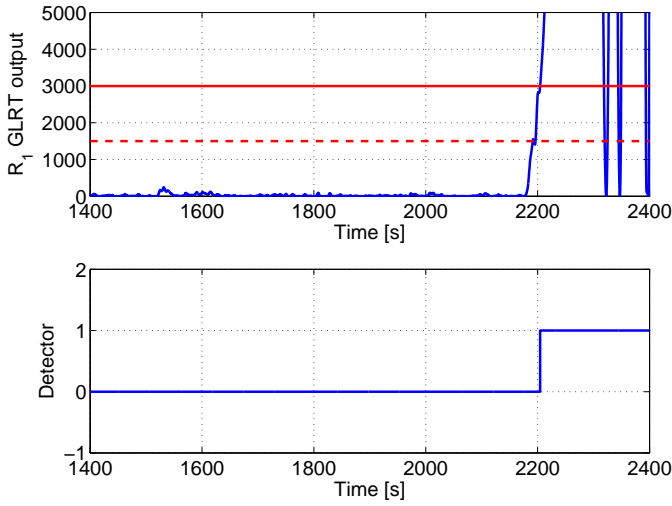
Fig. 14. GLRT output and decision signal from R_1. The alarm is raised at $t = 2204$ s. The solid horizontal line is the threshold for alarms and the dashed line is the threshold for stopping estimation.

Fig. 15. GLRT output and decision signal from R_2. The alarm is raised at $t = 2202$ s. The solid horizontal line is the threshold for alarms and the dashed line is the threshold for stopping estimation.
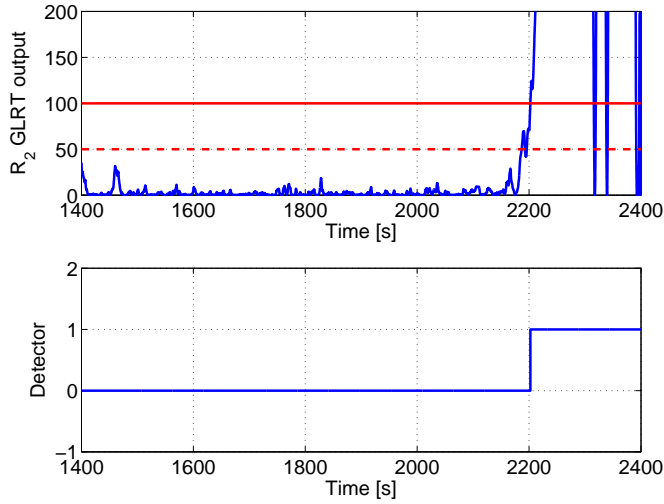
approaches for confirmation of reset to normal fall short when the aircraft makes maneuvers, when reaching the limits of flight envelope, where faulty readings of speed shortly coincide with the estimates. This is seen in the time-history plots as instants after the fault occurred where residuals cross zero at a certain rate to change sign and the GLRT detector(s) cross the detection threshold.

A. Residual zero-crossing

This phenomenon is caused by the residual value crossing zero and changing sign. For a short period of time $\mathcal{H}_0$ will be considered true if only the residual is considered. To cope with this issue, the derivative of the residual is also taken into account. The zero crossing is characterized by a high value of the residuals derivative which is different from what would happen if the residual went back to a zero value. The derivative of the residual can be estimated by the slope a straight line
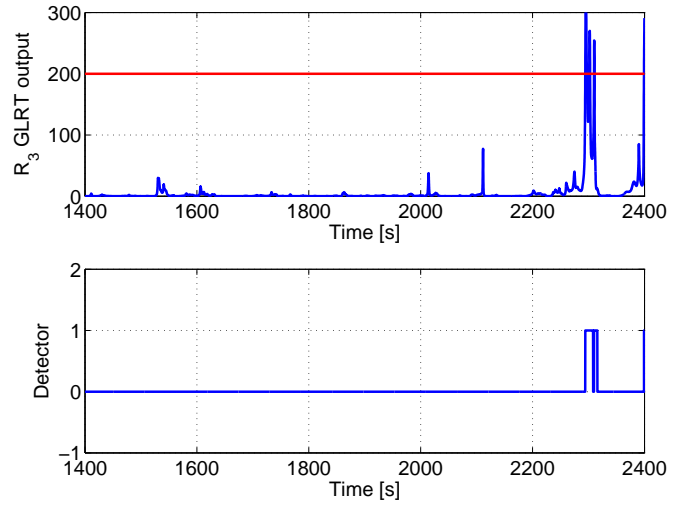

Fig. 16. GLRT output and decision signal from R_3.

approximation over a small window. Doing this moderates the noise influence.

Using least squares regression the derivative estimate over a window of size N is given by

$$\widehat{\dot{R}_1} = \frac{N \sum_{n \in N} t(n) R_1(n) - \sum_{n \in N} t(n) \sum_{n \in N} R_1(n)}{N \sum_{n \in N} t(n)^2 - \sum_{n \in N} t(n) \sum_{n \in N} t(n)}. \qquad (47)$$

The same expression is used to create $\widehat{\dot{R}_2}$. Combining the derivative with its matching residual in vector form $\boldsymbol{R_1} = \begin{bmatrix} R_1 & \widehat{\dot{R}_1} \end{bmatrix}^{\mathrm{T}}$ gives the desired properties.
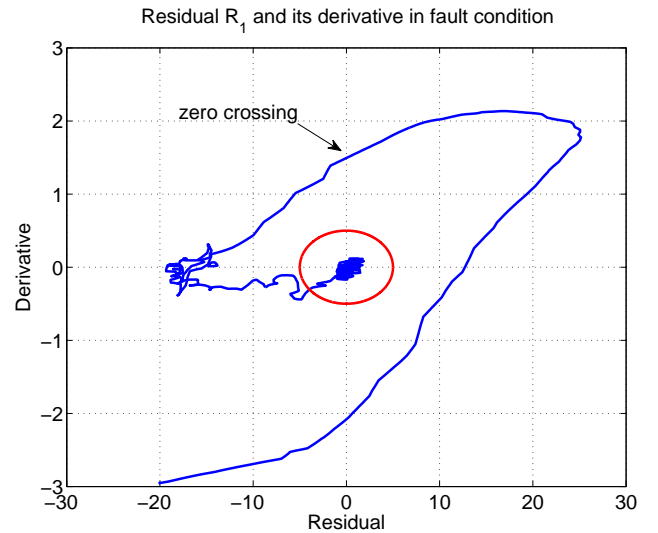

Fig. 17. Residual R_1 versus $\widehat{\dot{R}_1}$. The red ellipsis indicates the boundary of fault free behavior.

The trajectories of R_1 and $\widehat{\dot{R}_1}$ are shown in Fig. 17 for a time-slice before and after the fault occurs. An ellipsis in the center shows the part of the phase plane to which the signal should be within to be considered fault free.

The vector based detection is only used when the alarm is already raised to make to signal strongly detectable and not sensitive towards residual zero crossings. The vector based setup could be used in detecting faults but the derivative part is very sensitive to noise so the risk of false alarms would be greater. Since the scalar based setup is more robust this is used instead.

In most of the practical cases where a fault is discovered in the airspeed measurement system, the aircraft would be brought down in a controlled manner as quickly as possible. In these cases there is no value of being able to detect whether the system returns to a fault free state or not and therefore a suitable hysteresis curve around the residual would be enough to reject the zero crossings. However, in some cases the fault is due to icing of the pitot tube and reducing the altitude to a warmer level might recover from the fault. In this case it is essential to be certain that normal behavior is restored.

The formal test quantity R_4 is

$$\mathcal{H}_0: \quad R_4 = \left(\frac{R_1}{R_1^t}\right)^2 + \left(\frac{\widehat{\dot{R}_1}}{\dot{R}_1^t}\right)^2 \leq 1, \qquad (48)$$

where R_1^t and $\dot{R}_1^t$ are the axes of the ellipse constraining the normal operation range in Fig. 17. A formal change detection test is easily derived for R_4 to confirm return to normal. The condition from this test should be present simultaneously with the $\mathcal{H}_0$ from the GLRTs on R_1 to R_3 to confirm return to normal from an airspeed sensor fault.

X. Conclusion

Fault diagnosis of the airspeed measurement system for small fixed wing UAV's was considered in this paper. A diagnosis setup based on standard UAV sensor readings and a basic thrust model were suggested using ground speed from an onboard GPS unit. Two supplemental estimates of air speed were obtained to calculate residuals. Wind speed and direction were estimated to provide one such estimate when adding the ground speed vector. The second airspeed estimate was obtained from thrust-speed curves employing a non-linear adaptive observer to estimate the engine thrust.

A hypothesis test based on GLRT was designed using past flight-data recordings to find detection thresholds to give desired low probability of false alarms. Tuning, in this way, to the physical noise and disturbances on the aircraft, this ensured a very low false alarm rate. Detection probability was analyzed from flight data where a genuine fault occurred and detector design was suggested to be based on balancing estimated false alarm and detection probabilities. For a recorded case of a genuine fault, that later caused a crash of the UAV, detection was obtained with 85% of the data exceeded the chosen threshold after the anticipated onset.

The method was verified both using simulated faults and the real data from an UAV lost due to an airspeed sensor fault. The simulation shows that, with the false alarm rate chosen, that speed sensor faults exceeding 6.5 m/s are guaranteed detectable, which was judged to be an acceptable level that can be handled within robustness limits for conventional autopilot controls. With false alarm rate below $0.003/\text{h}$ with normal wind disturbances, detection of the real life fault was achieved 130 s before radio contact was lost with the aircraft. This time window would leave ample time for the operator to react and bring the aircraft down safely.

References

[1] A. Tornambé, "Use of asymptotic observers having high-gains in the state and parameters estimation," in *Proceedings of the 28th Conference on Decision and Control*, 1989.

[2] Y. M. Cho and R. Rajamani, "A systematic approach to adaptive observer synthesis for nonlinear systems," *IEEE Transactions on Automatic Control*, vol. 42, no. 4, pp. 534–537, April 1997.

[3] L. Ljung, "Asymptotic behavior of the extended kalman filter as a parameter estimator for linear systems," *IEEE Transactions on Automatic Control*, vol. 24 (1), pp. 36–50, 1979.

[4] W.-w. Zhou and M. Blanke, "Identification of a class of non-linear state space models using rpe techniques," *IEEE Transactions of Automatic Control*, vol. 34 (3), pp. 312–316, 1989.

[5] C. Edwards, S. K. Spurgeon, and R. Patton, "Sliding mode observers for fault detection and isolation," *Automatica*, vol. 36, pp. 541–553, 2000.

[6] M. Blanke, R. Izadi-Zamanabadi, and T. Lootsma, "Fault monitoring and re-configurable control for a ship propulsion plant," *Journal of Adaptive Control and Signal Processing*, vol. 12, pp. 671–688, 1998.

[7] C. Edwards, T. J. J. Lombaerts, and M. H. Smaili, Eds., *Fault Tolerant Flight Control: A Benchmark Challenge*. Springer, 2010.

[8] X. Yu and J. Jiang, "Hybrid fault-tolerant flight control system design against partial actuator failures," *IEEE Transactions on Control Systems Technology*, vol. 20 (4), pp. 871–886, 2012.

[9] H. Wagner, G. Nikolov, A. Bierig, and H. Spangenberg, "Challenges for health monitoring of electromechanical flight control actuation systems," *SAE International Journal of Aerospace*, vol. 4 (2), pp. 1315–1327, 2011.

[10] A. Zolghadri, "Advanced model-based fdir techniques for aerospace systems: Today challenges and opportunities," *Progress in Aerospace Sciences*, vol. 53, pp. 18–29, 2012.

[11] J. Marzat, H. Piet-Lahanier, F. Damongeot, and E. Walter, "Model-based fault diagnosis for aerospace systems: a survey," *Journal of Aerospace Engineering*, vol. 226, no. 10, pp. 1329–1360, 2012.

[12] P. Goupil, "Airbus state of the art and practices on fdi and ftc in flight control system," *Control Engineering Practice*, vol. 19 (6), pp. 524 – 539, 2011.

[13] G. Ducard and H. P. Geering, "Efficient nonlinear actuator fault detection and isolation system for unmanned aerial vehicles," *Journal of Guidance, Control, and Dynamics*, vol. 31 (1), pp. 225–237, 2008.

[14] G. J. J. Ducard, *Fault-tolerant Flight Control and Guidance Systems*. Springer Verlag, 2009.

[15] F. Bateman, H. Noura, and M. Ouladsine, "Fault diagnosis and fault-tolerant control strategy for the aerosonde uav," *IEEE Transactions on Aerospace and Eelectronic Systems*, vol. 47 (3), pp. 2119–2137, 2011.

[16] M. L. Fravolini, V. Brunori, G. Campa, M. R. Napolitano, and M. La Cava, "Structured analysis approach for the generation of structured residuals for aircraft fdi," *IEEE Transactions on Aerospace and Electronic Systems*, vol. 45 (4), pp. 1466–1482, 2009.

[17] E. Alcorta-Garcia, A. Zolghadri, and P. Goupil, "A nonlinear observer-based strategy for aircraft oscillatory failure detection: A380 case study," *IEEE Transactions on Aerospace And Electronic Systems*, vol. 47 (4), pp. 2792–2806, 2011.

[18] I. Samy, I. Postlethwaite, and D.-W. Gu, "Unmanned air vehicle air data estimation using a matrix of pressure sensors: a comparison of neural networks and look-up tables," *Journal of Aerospace Engineering*, vol. 225 (7), pp. 807–820, 2011.

[19] T. J. Wheeler, P. Seiler, A. K. Packard, and G. J. Balas, "Performance analysis of fault detection systems based on analytically redundant linear time-invariant dynamics," in *Proc. 2011 American Control Conference (ACC 2011)*, 2011, pp. 214–219.

[20] Bureau d'Enquêtes et d'Analyses pour la sécurité de l'aviation civile, "Final Report On the accident on 1st June 2009 to the Airbus A330-203 registered F-GzCP operated by Air France flight AF 447 Rio de Janeiro - Paris," Ministère de l'Écologie, du Développement durable, des Tarnsports et du Logement, Tech. Rep., 2012. [Online]. Available: http://www.bea.aero/docspa/2009/f-cp090601.en/pdf/f-cp090601.en.pdf

[21] S. Hansen, M. Blanke, and J. Adrian, "Diagnosis of uav pitot tube defects using statistical change detection," in *7th Symposium on Intelligent Autonomous Vehicles*, 2010.

[22] Meggitt Defence Systems Ltd., "Banshee aerial target system," 2008. [Online]. Available: http://www.meggittdefenceuk.com/PDF/Banshee aerial target system.pdf

[23] A. Bateman, D. Ward, J. Monaco, and Z. Lin, "Stability analysis for reconfigurable systemn with actuator saturation," in *Proc. American Control Conference, Anchorage, AK*, 2002, pp. 4783–4788.

[24] E. P. Lesley, "Propeller tests to determine the effect of number of blades at two typical solidities," National Advisory Committee For Aeronautics, Tech. Rep., 1939.

[25] H. D. Nissen, "Instrumentation and control of unmanned air vehicle," Ph.D. dissertation, Technical University of Denmark, 2002.

[26] M. Blanke, "Ship propulsion losses related to automatic steering and prime mover control," Ph.D. dissertation, Technical University of Denmark, 1981.

[27] A. Cho, J. Kim, S. Lee, and C. Kee, "Wind estimation and airspeed calibration using a uav with a single-atenna gps receiver and pitot tube," *IEEE Transactions on Aerospace and Electronic Systems*, vol. 47, pp. 109–117, 2011.

[28] R. G. Brown and P. Y. C. Hwang, *Introduction to Random Signals and Applied Kalman Filtering*. John Wiley & Sons, 1997.

[29] B. L. Stevens and F. L. Lewis, *Aircraft Control and Simulation*, 2nd ed. John Wiley & Sons, 2003.

[30] F. Gustafsson, *Adaptive filtering and change detection*. John Wiley & Sons, 2000.

[31] H. Jamouli, D. Sauter, and J.-Y. Keller, "A new adaptive kalman estimator for detection and isolation of multiple faults using modified glr test," in *Conf. on Control and Fault Tolerant Systems*, Nice, October 2010, pp. 76–81.

[32] A. S. Willsky and H. L. Jones, "A generalized likelihood ratio approach to detection and estimation of jumps in linear systems," *IEEE Transactions on Automatic Control*, vol. 21, pp. 108–112, 1976.

[33] S. M. Kay, *Fundamentals of Statistical Signal Processing: Detection Theory*. Prentice-Hall PTR, 1998.

[34] J. Dong, M. Verhaegen, and F. Gustafsson, "Robust fault detection with statistical uncertainty in identified parameters ." *IEEE Transactions on Signal Processing*, vol. 60 (10), pp. 5064–5072, 2012.

[35] R. Galeazzi, M. Blanke, and N. K. Poulsen, "Early detection of parametric roll resonance on container ships," *IEEE Transactions on Control Systems Technology*, 2013.

[36] S. Fang, M. Blanke, and B. J. Leira, "Mooring system diagnosis and structural reliability control for position moored vessels," *Control engineering Practice*, 2013.

[37] Q. Zhao and M. Kinnaert, "Statistical properties of cusum based fault detection schemes for fault tolerant control," in *Proc. 48th IEEE Conference on Decision and Control*, 2009, pp. 7831–7836.

[38] F. Gustafsson and J. Palmqvist, "Change detection design for low false alarm rates," in *IFAC International Symposium on Fault Detetction, Supervision and Safety for Technical Processes (SAFEPROCESS'97)*, 1997, pp. 1017–1022.

[39] G. Verdier and N. H. A. J.-P. Vila, "Adaptive threshold computation for cusum-type procedures in change detection and isolation problems," *Computational Statistics and Data Analysis*, vol. 52, pp. 4161–4174, 2008.

[40] N. E. Wu, "Coverage in fault-tolerant control," *Automatica*, vol. 40, pp. 537–548, 2004.

[41] N. E. Wu, S. Thavamani, Y. Zhang, and M. Blanke, "Sensor fault masking of a ship propulsion system," *Control Engineering Practice*, vol. 14, pp. 1337–1345, 2006.

[42] T. Perez, A. Donaire, P. de Lamberterie, and B. Williams, "A framework for testing robust autonomy of uas during design and certification," in *AIAA Infotech@Aerospace Conference and Exhibit*, vol. 1, 2011, pp. 303–315.

[43] H. K. Khalil, *Nonlinear Systems*, 3rd ed. Prentice Hall, 2002.

APPENDIX

A. Reference frames

1) Earth fixed earth centred frame (ECEF): A right-hand frame with origin at the Earth center. The x-axis is extended through the intersection between the prime-median and Equator and the z-axis points towards the north pole. GPS measurements are given in this system.

2) Vehicle carried earth frame: Standard North, East, Down system following the air vehicle around on the surface on the earth reference ellipsoid.

3) Body frame: The axes are coinciding with the aircraft body regardless of attitude and has origin in the aircraft center of mass. The x-axis is forward through the aircraft's nose, the y-axis to the right, and the z-axis pointing out of the belly.

4) Wind frame: Is centered at the aircraft's center of mass, and has its x-axis along the relative direction of wind. The angle of attack α and the side slip angle β describe a rotation from wind frame to body frame.

B. Observer Stability Proof

The lower bound for the observer gain is derived in this section. To start with the gain functions used for the adaptive parameters Θ_{uu} and $\Theta_{uu\alpha}$ are assumed Lipschitz according to the following relations

$$\|F_1(u,t) - F_1(\bar{u},t)\| \leq \gamma_1 \|u - \bar{u}\|, \qquad (49)$$

$$\|F_2(u,t) - F_2(\bar{u},t)\| \leq \gamma_2 \|u - \bar{u}\|. \qquad (50)$$

The assumptions in (49) and (50) is valid because the physical values of the aircraft are bounded in the following way

$$
\begin{aligned}
u &\in [0; u_{max}], \\
\alpha &\in [\alpha_{min}; \alpha_{max}], \\
n &\in [0; n_{max}].
\end{aligned}
$$

Applying the expressions for $F_1(u,t)$ and $F_2(u,t)$ in (31) the following Lipschitz constants are found

$$\gamma_1 = \frac{\varrho S u_{max}}{m}, \quad \gamma_2 = \frac{\varrho S \alpha_{max} u_{max}}{m}. \qquad (51)$$

For the observer to be asymptotic stable the error $\tilde{x} = x - \hat{x} = 0$. For this to be true a Lyapunov function $\mathcal{V}(\tilde{x})$ must satisfy theorem 4.8 in [43]. This states that the following must be satisfied.

1) Uniform asymptotic stability: Let $x = 0$ be an equilibrium point for $\dot{x} = f(x,t)$ and $D \subset \mathbb{R}^n$ be a domain containing $x = 0$. Let $\mathcal{V} : [0;\infty[\times D \to \mathbb{R}$ be a continuously differentiable function such that

$$W_1(x) \leq \mathcal{V}(x,t) \leq W_2(x) \qquad (52)$$

and

$$\frac{\partial \mathcal{V}}{\partial t} + \frac{\partial \mathcal{V}}{\partial x} f(x,t) \leq 0, \qquad (53)$$

$\forall t \geq 0$ and $\forall x \in D$ where $W_1(x)$ and $W_2(x)$ are continuous positive definite functions on D. Then, $x = 0$ is uniformly asymptotically stable.

The following function is chosen as a Lyapunov function candidate

$$\mathcal{V}(\tilde{x},t) = \tilde{x}^{\mathrm{T}} P \tilde{x}, \qquad (54)$$

where P is a diagonal matrix with trace $[a,b,c]$ where a, b and c are elements of size 1 with units to allow addition of the terms in the quadratic form Eq. 54. These unit conversion factors are disregarded in the derivation below.

$$\mathcal{V}(\tilde{x},t) = \tilde{x}^{\mathrm{T}} \tilde{x} = \tilde{u}^2 + \tilde{\Theta}_{uu}^2 + \tilde{\Theta}_{uu\alpha}^2. \qquad (55)$$

Choosing the positive definite functions

$$W_1(\tilde{x}) = \tfrac{1}{2}\mathcal{V}(\tilde{x}, t) \qquad \text{and} \qquad W_2(\tilde{x}) = 2\mathcal{V}(\tilde{x}, t),$$

satisfy (52). The time derivative of $\mathcal{V}(\tilde{x})$ is zero because no explicit time dependence is present

$$\frac{\partial \mathcal{V}}{\partial t} = 0. \tag{56}$$

The state derivative of $\mathcal{V}(\tilde{x})$ is

$$\begin{aligned}
\frac{\partial \mathcal{V}}{\partial \tilde{x}} \boldsymbol{f}(\tilde{x}, t) &= \begin{bmatrix} 2\tilde{u} & 2\tilde{\Theta}_{uu} & 2\tilde{\Theta}_{uu\alpha} \end{bmatrix} \boldsymbol{f}(\tilde{x}, t) \quad (57) \\
&= 2\tilde{u}\dot{\tilde{u}} + 2\tilde{\Theta}_{uu}\dot{\tilde{\Theta}}_{uu} + 2\tilde{\Theta}_{uu\alpha}\dot{\tilde{\Theta}}_{uu\alpha}.
\end{aligned}$$

From this (53) becomes

$$2\tilde{u}\dot{\tilde{u}} + 2\tilde{\Theta}_{uu}\dot{\tilde{\Theta}}_{uu} + 2\tilde{\Theta}_{uu\alpha}\dot{\tilde{\Theta}}_{uu\alpha} \leq 0. \tag{58}$$

The expression for $\dot{\tilde{u}}$ given in (35) was

$$\begin{aligned}
\dot{\tilde{u}} = & \left(\frac{T_{nu}n}{m} - L \right) \tilde{u} + F_1(u, t)\Theta_{uu} \quad (59) \\
& - F_1(\hat{u}, t)\hat{\Theta}_{uu} + F_2(u, t)\Theta_{uu\alpha} - F_2(\hat{u}, t)\hat{\Theta}_{uu\alpha}
\end{aligned}$$

Inserting in (58)

$$2\tilde{u}\left(\left(\frac{T_{nu}n}{m} - L \right) \tilde{u} + F_1(u, t)\Theta_{uu} \right. \tag{60}$$
$$-F_1(\hat{u}, t)\hat{\Theta}_{uu} + F_2(u, t)\Theta_{uu\alpha} - F_2(\hat{u}, t)\hat{\Theta}_{uu\alpha} \Big)$$
$$+ 2\tilde{\Theta}_{uu}\dot{\tilde{\Theta}}_{uu} + 2\tilde{\Theta}_{uu\alpha}\dot{\tilde{\Theta}}_{uu\alpha}.$$

This gives

$$2\tilde{u}\left(\left(\frac{T_{nu}n}{m} - L \right) \tilde{u} + F_1(u, t)\Theta_{uu} - F_1(\hat{u}, t)\Theta_{uu} \right. \tag{61}$$
$$+ F_2(u, t)\Theta_{uu\alpha} - F_2(\hat{u}, t)\Theta_{uu\alpha} \Big)$$
$$+ 2\tilde{\Theta}_{uu}\dot{\tilde{\Theta}}_{uu} + 2\tilde{\Theta}_{uu\alpha}\dot{\tilde{\Theta}}_{uu\alpha}$$
$$+ 2\tilde{u}F_1(\hat{u}, t)\tilde{\Theta}_{uu} + 2\tilde{u}F_2(\hat{u}, t)\tilde{\Theta}_{uu\alpha}$$
$$\leq 2\tilde{u}\left(\left(\frac{T_{nu}n}{m} - L \right) \tilde{u} + \gamma_1 \|\tilde{u}\| \max\left(\|\Theta_{uu}\| \right) \right.$$
$$+ \gamma_2 \|\tilde{u}\| \max\left(\|\Theta_{uu\alpha}\| \right) \Big).$$

As seen above having the adaptive gains as functions F_1 and F_2 as suggested in [2] simplifies the derivation significantly. The above equation should according to (53) be compared to

$$2\tilde{u}\left(\left(\frac{T_{nu}n}{m} - L \right) \tilde{u} + \gamma_1 \|\tilde{u}\| \max\left(\|\Theta_{uu}\| \right) \right. \tag{62}$$
$$+ \gamma_2 \|\tilde{u}\| \max\left(\|\Theta_{uu\alpha}\| \right) \Big) \leq$$
$$2\tilde{u}^2 \left(\frac{T_{nu}n}{m} - L + \gamma_1 \max\left(\|\Theta_{uu}\| \right) \right.$$
$$+ \gamma_2 \max\left(\|\Theta_{uu\alpha}\| \right) \Big) \leq$$
$$\frac{T_{nu}n}{m} - L + \gamma_1 \max\left(\|\Theta_{uu}\| \right)$$
$$+ \gamma_2 \max\left(\|\Theta_{uu\alpha}\| \right) \leq 0.$$

From this it is seen that the gain L should satisfy the following inequality in order for the observer to be uniform asymptotically stable

$$L \geq \frac{T_{nu}n_{max}}{m} + \gamma_1 \max\left(\|\Theta_{uu}\| \right) + \gamma_2 \max\left(\|\Theta_{uu\alpha}\| \right). \tag{63}$$

Inserting the maximum value for the worst case the gain ends up being

$$L \geq \frac{T_{nu}n_{max} + \varrho S u_{max} \left(\max\left(\|\Theta_{uu}\| \right) + \alpha \max\left(\|\Theta_{uu\alpha}\| \right) \right)}{m}. \tag{64}$$

The derivation above also holds for the case where $\Theta_{uu\alpha} = 0$.

Søren Hansen received the MScEE degree in 2009 and the PhD entitled "Fault Diagnosis and Fault Handling for Autonomous Aircraft" was obtained in Jan. 2013 both from the Technical University of Denmark, DTU. He is now assistant prof. at DTU. His research interests are robots and autonomous vehicles with emphasis on fault diagnosis and fault tolerance.

Mogens Blanke (M 1974, SM 1985) received the MScEE degree in 1974 and the PhD degree in 1982 from the Technical University of Denmark, DTU. He was Systems Analyst with the European Space Agency 1975–76, with DTU 1977-84, was Head of Division at Lyngsø Marine 1985-89, Professor at Aalborg University 1990–99. He is now (2000 –) Professor in Automation and Control at DTU and since 2005 also Adjunct Professor at the Norwegian University of Science and Technology. His research interests are automation and control in general and diagnosis and fault tolerant control as his area of special focus. Application areas include autonomous vehicles in space, air, on land and in the marine environment.

Prof. Blanke has held various positions in the International Federation of Automatic Control, including founding member and first Chair of the Technical Committee on Marine Systems, Coordinating Committee Chair and Member of Council. He is also a member of the IFAC SAFEPROCESS Technical Committee. He is Associate Editor for Control Engineering Practice and Technical Editor for IEEE Transactions of Aerospace and Electronic Systems.